Electrically detected magnetic resonance (EDMR) spectroscopy of introduced spin defects in silicon carbide for quantum magnetometry

Daniel R. Hart[1, 2], Deval M. Deliwala[3], Ryan Byrne[4], and David J. Spry[5]

[1]Optics and Photonics Branch, NASA Glenn Research Center, Cleveland, OH 44135
[2]Department of Physics and Mathematics, Southern University and A & M College, Baton Rouge, LA 70813
[3]Department of Physics, University of California-Berkeley, Berkeley, CA 94720
[4]School of Applied and Engineering Physics, Cornell University, Ithaca, NY 14850
[5]Smart Sensing and Electronics Systems Branch, NASA Glenn Research Center, Cleveland, OH 44135

ABSTRACT

Quantum sensing offers a path toward compact self-calibrating magnetometers for heliophysics and planetary missions, where conventional field probes struggle with size, weight, power, and radiation tolerance. The Quantum Sensing and Spin Physics (Q-SASP) laboratory at NASA is addressing these limitations by exploiting spin defects in SiC diodes and reading them out via electrically detected magnetic resonance (EDMR) and near-zero-field magnetoresistance (NZFMR). Here, we present a comprehensive resonance-to-resonance simulation of EDMR signatures arising from the negatively charged silicon vacancy in 4H-SiC. The model reproduces the experimental spectral response and quantitatively demonstrates that spin-dependent recombination pathways primarily govern magnetometric sensitivity and overall device performance. Additionally, we characterize the power-dependent traits of resonance features to demonstrate how RF drive conditions affect signal amplitudes and linewidths while highlighting practical operating regimes for device operation.

Keywords: spin defect, EDMR, NZFMR, quantum sensing, magnetometry, silicon carbide

1. INTRODUCTION

High-fidelity magnetic field sensing supports diverse technologies, from aircraft icing-phase monitors [1] and neuronal current mapping in biological specimens [2] to global planetary-field surveys [3,4]. Achieving the required sub-μT resolution while satisfying size, weight, power, and radiation-tolerance constraints pushes conventional flux-gate and Hall probes to their limits. Solid-state quantum sensors based on point defects in wide-band-gap semiconductors offer an attractive path forward.

Silicon carbide (SiC) is a particularly promising host: its low spin–orbit coupling and sparse nuclear spins suppress magnetic noise, enabling long spin-coherence times at room temperature [5]. Optically active defects such as the neutral divacancy (VV^0) [6,7] and the negatively charged silicon vacancy V_{Si}^- [8–10] exhibit spin-dependent near-infrared fluorescence and have even been proposed for quantum-communication links [11,12]. Established SiC fabrication methods make it possible to embed these centers in photonic resonators that boost collection efficiencies [13] and waveguides that route emission on-chip [14]. Deep-level defects that lack a spin degree of freedom are also valuable as single-photon sources for quantum key-distribution protocols or as electrically addressable emitters for integrated optoelectronics [15–17]. The same material platform therefore supports both *quantum communication* and *quantum sensing*. Although optically detected magnetometry has advanced rapidly, the prospect of *electrical* read-out, via ionization-initiated defect states, could further simplify instrumentation and facilitate monolithic integration with existing Si/SiC electronics. Initial analysis suggests that sensitivities in the several-hundred-pT $\mathrm{Hz}^{-1/2}$ regime are within reach [3], leaving ample headroom for future improvement.

1.1 Spin Hamiltonian, Zeeman Response, and Field Sensitivity

The spin dynamics of a point defect with total spin S are governed by the *Spin Hamiltonian*

$$\hat{H} = \mu_B \, \mathbf{B}_0 \cdot \mathbf{g} \cdot \mathbf{S} + \mathbf{S} \cdot \mathbf{A} \cdot \mathbf{I} + \mathbf{S} \cdot \mathbf{D} \cdot \mathbf{S} + \mathbf{S} \cdot \mathbf{J} \cdot \mathbf{S}, \tag{1}$$

where μ_B is the Bohr magneton, $\mathbf{g}$ the Zeeman tensor, $\mathbf{A}$ the hyperfine tensor, $\mathbf{D}$ the second-rank crystal-field tensor (non-zero for $S \geq 1$) [20], and $\mathbf{J}$ the exchange tensor. In the high-field limit $g\mu_B B_0 \gg \max\{\|\mathbf{D}\|, \|\mathbf{A}\|\}$, the energy levels separate linearly,

$$\nu(B_0) = \frac{g\mu_B}{h} \, B_0, \qquad \frac{\partial \nu}{\partial B_0} = \frac{g\mu_B}{h} \approx 28 \text{ MHz G}^{-1}, \tag{2}$$

so a frequency shift $\delta\nu$ maps directly onto a field change $\delta B_0 = h \, \delta\nu / (g\mu_B)$.

1.2 Spin-Dependent Recombination and EDMR

Lépine's pioneering experiment on silicon diodes showed that resonant spin flips can modulate photocurrent, inaugurating *electrically detected magnetic resonance* (EDMR) [21]. The believed primary mechanism is *spin-dependent recombination* (SDR): triplet electron-hole pairs live far longer than singlets, so microwaves that mix the two manifolds change the steady-state carrier population. The Kaplan–Solomon–Mott model [22] predicts the relative current change

$$\frac{\Delta I}{I_0} \;\approx\; \eta \, \frac{P_{\text{rf}}}{1 + P_{\text{rf}}/P_{\text{sat}}}, \tag{3}$$

with efficiency η and saturation power P_{sat}. State-of-the-art devices can register the signal of fewer than one hundred donors [23], implying formidable magnetometric potential when combined with the Zeeman response of Equation (2).

1.3 Near-Zero-Field Magnetoresistance (NZFMR)

When Zeeman and hyperfine energies are comparable ($B_0 \lesssim 1$ G), the singlet and triplet subspaces mix intrinsically, yielding a purely electrical magnetoresistance

$$\Delta I(B_0) \propto \frac{B_0^2}{B_0^2 + B_{\text{hf}}^2}, \quad \left| \frac{dI}{dB_0} \right|_{\max} = \frac{\Delta I}{2B_{\text{hf}}}, \tag{4}$$

where B_{hf} is the root-mean-square hyperfine field. Because B_{hf} is set by immutable nuclear moments, the line center furnishes an intrinsic, drift-free frequency reference ideally suited to multi-year space missions. Sub-μT sensitivities have already been achieved in commercial 4H-SiC Schottky diodes at 500°C without microwaves or optics [24].

1.4 The Negatively Charged Silicon Vacancy

The monovacancy V_{Si}^- in 4H-SiC is a quartet ($S = 3/2$) whose axial crystal-field parameter is $D \approx 35$ MHz [25], enabling on-chip radio-frequency control. Room-temperature coherence times exceed 100 μs [26], and vector magnetometry has already been demonstrated under ambient conditions [27]. Its thermal resilience, radiation hardness, and full compatibility with SiC microfabrication make V_{Si}^- a leading candidate for compact magnetometers on heliophysics and planetary missions.

1.5 Scope and Contributions

Here we perform a resonance-to-resonance simulation of V_{Si}^- EDMR in 4H-SiC, extracting the tensor parameters of Equation (1) and propagating them into the low-field description of Equation (4). The resulting NZFMR lineshape and sensitivity predictions therefore link microscopic spin physics directly to the practical requirements of NASA's next-generation, self-calibrating quantum magnetometers. Additionally, we chart how hyperfine sidebands broaden and saturate with RF power, supplying empirical benchmarks that for future simulation validation and highlight optimal operating regimes for device deployment.

2. SIMULATING THE SILICON VACANCY FOR EDMR

2.1 Model Hamiltonian

The negatively charged silicon vacancy (V_{Si}^{-}) in 4H-SiC is modeled as two $S = \frac{1}{2}$ electrons $(\mathbf{S}_1, \mathbf{S}_2)$ coupled to one ^{29}Si and one ^{13}C nuclear spin $(\mathbf{I}_{\mathrm{Si}}, \mathbf{I}_{\mathrm{C}})$. The composite Hilbert space

$$\mathscr{H} \;=\; \big(\tfrac{1}{2}\text{–electron}\big)^{\otimes 2} \;\otimes\; \big(\tfrac{1}{2}\text{–nucleus}\big)^{\otimes 2}, \qquad \dim \mathscr{H} = 2^4 = 16.$$

The static spin Hamiltonian is a linear operator on the 16-dimensional Hilbert space:

$$\mathcal{H}_{\mathrm{spin}} \;\in\; \mathcal{L}(\mathscr{H}), \qquad \mathscr{H} \;\cong\; \mathbb{C}^{16}.$$

It can be decomposed as the combination of four Hamiltonians:

$$\mathcal{H}_{\mathrm{spin}} = \hat{H}_Z + \hat{H}_{\mathrm{hf}} + \hat{H}_{\mathrm{ZFS}} + \hat{H}_{\mathrm{ex}},$$

where

$$\begin{aligned}
\hat{H}_Z &= \mu_B \mathbf{B}_0 \cdot \mathbf{g}_e \cdot (\mathbf{S}_1 + \mathbf{S}_2) + \gamma_{\mathrm{Si}}\, \mathbf{B}_0 \cdot \mathbf{I}_{\mathrm{Si}} + \gamma_{\mathrm{C}}\, \mathbf{B}_0 \cdot \mathbf{I}_{\mathrm{C}}, \\
\hat{H}_{\mathrm{hf}} &= \mathbf{S}_1 \cdot \mathbf{A}_{\mathrm{Si}} \cdot \mathbf{I}_{\mathrm{Si}} + \mathbf{S}_2 \cdot \mathbf{A}_{\mathrm{C}} \cdot \mathbf{I}_{\mathrm{C}}, \\
\hat{H}_{\mathrm{ZFS}} &= \mathbf{S}_1 \cdot \mathbf{D} \cdot \mathbf{S}_2, \qquad \big\|\mathbf{D}\big\| \simeq 35 \text{ MHz}, \\
\hat{H}_{\mathrm{ex}} &= J\, \mathbf{S}_1 \cdot \mathbf{S}_2, \qquad J \lesssim \text{kHz (weak)}.
\end{aligned}$$

All operators can be expressed in the coupled $\{|s, m\rangle \otimes |m_{I,\mathrm{Si}}, m_{I,\mathrm{C}}\rangle\}$ basis, and symbolic implementation lets B_0 and tensor parameters vary at runtime.

2.2 Spin-dependent recombination kinetics

To link spin dynamics to EDMR, we embed the Hamiltonian in a modified steady-state stochastic Liouville equation adapted from [38]:

$$0 = -\frac{i}{\hbar}\,[\mathcal{H}_{\mathrm{spin}}, \rho] - \frac{k_{\mathrm{S}} + k_{\mathrm{D}}}{2}\,\{\Lambda_{\mathrm{S}}, \rho\} - \frac{k_{\mathrm{D}}}{2}\,\{\Lambda_{\mathrm{T}}, \rho\} + \frac{p}{16}\,\Gamma, \tag{5}$$

where curly brackets denote the anticommutator, Λ_{S} (Λ_{T}) projects onto the singlet (triplet) electronic subspace, k_{S} and k_{D} are the singlet-recombination and triplet–dissociation rates, p is the spin-pair generation rate, and Γ is the 16×16 identity. Because only singlet states recombine (and hence change the current) due to spin-selection rules, the EDMR current is proportional to the steady-state singlet population,

$$I(B_0) = A\,\mathrm{Tr}(\Lambda_{\mathrm{S}}\rho) + I_0,$$

where A and I_0 are global scaling constants.

2.3 Accelerated Lyapunov solver

Equation (5) can be cast into Lyapunov form $A\rho + \rho A^{\dagger} + g = 0$, with

$$A = -\frac{i}{\hbar}\,\mathcal{H}_{\mathrm{spin}} - \tfrac{1}{2}(k_{\mathrm{S}} + k_{\mathrm{D}})\Lambda_{\mathrm{S}} - \tfrac{1}{2}\,k_{\mathrm{D}}\Lambda_{\mathrm{T}}, \qquad g = -\tfrac{p}{16}\,\Gamma.$$

Vectorizing ρ via $\mathrm{vec}(A\rho + \rho A^{\dagger}) = \big(I \otimes A + A^{\dagger T} \otimes I\big)\mathrm{vec}\rho$ yields a 256×256 linear system solved once per B_0 value with a cache-aware LU factorization (200-point sweep, –100 G $\rightarrow$ +100 G: $\sim$200 ms on a single M3 core).

2.4 Microwave drive and rotating frame

A transverse field $\hat{H}_{\mathrm{drive}}(t) = \hbar\omega_1 \cos(2\pi\nu t) S_x$ is carried to the rotating frame; after applying the rotating-wave approximation, only $\hat{H}_{\mathrm{RWA}} = \frac{\hbar\omega_1}{2} S_x$ survives. The dressed-state Rabi frequency is $\Omega = \sqrt{(\omega - \omega_0)^2 + \omega_1^2}$, so the full spin Hamiltonian becomes $\mathcal{H}_{\mathrm{spin}} = \hat{H}_{\mathrm{static}} + \hat{H}_{\mathrm{RWA}}$.

2.5 Lock-in reconstruction

For a sinusoidal field modulation $B_{\mathrm{pp}} \cos \omega_{\mathrm{m}} t$ of peak-to-peak amplitude $B_{\mathrm{pp}} = 2$ G, the ideal first-harmonic lock-in signal is

$$V_1(B_0) = \frac{2}{B_{\mathrm{pp}}} \frac{1}{2\pi} \int_0^{2\pi} I\Big(B_0 + \tfrac{B_{\mathrm{pp}}}{2} \sin\phi\Big) \sin\phi \, \mathrm{d}\phi.$$

When B_{pp} is much smaller than the intrinsic linewidth, the integral reduces to the familiar derivative relation

$$V_1 \;\approx\; \frac{B_{\mathrm{pp}}}{4} \frac{\partial I}{\partial B} \,. \tag{6}$$

The integral is evaluated numerically by sampling the modulation *phase* over one complete cycle:

$$\phi_j = \frac{2\pi j}{n_\phi}, \qquad j = 0, 1, \ldots, n_\phi - 1,$$

with $n_\phi = 256$ uniformly spaced points. A Riemann-sum approximation yields

$$V_1(B_0) \;\approx\; \frac{2}{B_{\mathrm{pp}}\, n_\phi} \sum_{j=0}^{n_\phi - 1} I\Big(B_0 + \tfrac{B_{\mathrm{pp}}}{2} \sin\phi_j\Big) \sin\phi_j.$$

This discrete formulation reproduces both the amplitude and the phase of the first-harmonic lock-in response.

2.6 Parameter set and validation

Tensor parameters $\left[\mathbf{g}_e, \mathbf{A}_{\mathrm{Si}}, \mathbf{A}_{\mathrm{C}}, \mathbf{D}, J\right]$ are adopted from literature, whereas kinetic rates $(k_{\mathrm{S}}, k_{\mathrm{D}}, p)$ and scaling constants (A, I_0) come from a least-squares fit to a 3 V, 200 MHz, 2 G-modulated reference spectrum. The simulation reproduces the central NZFMR peak and hyperfine satellites at ± 71.4 G, as shown in Figure (1). If modulation is disabled, the raw spectrum (bottom panel) reveals the resonance manifold.

3. EMPIRICAL ANALYSIS OF POWER-DEPENDENT SIGNAL CHARACTERISTICS

EDMR spectra often contain several partially overlapping resonances as well as experimental artifacts, both of which can obscure the underlying spin physics and depress the signal-to-noise ratio. To address these issues in 4H-SiC, we (i) optimize the lock-in reference phase in post-processing, (ii) extract signal features with a parametric line-shape model, and (iii) quantify the RF-power dependence of those features.

3.1 Reference-phase optimization

In our setup the electrical current change is detected with a lock-in amplifier (LIA): the external field is modulated and the in-phase (I) and quadrature (Q) components are recorded. Ideally, a pure spin-dependent signal lies along the in-phase axis in the I–Q plane. We determine that axis *a posteriori* by applying principal component analysis (PCA) to the I–Q data for each field sweep; the first principal component, dominated by the resonant contribution, defines the correct reference phase, after which the data are rotated accordingly.

Non-resonant artifacts, notably RF heating, generally exhibit a different phase and therefore populate the orthogonal PCA component. In practice, we see that these artifacts appear with a phase lag close to 90° and are cleanly isolated in the quadrature channel after rotation. Future work will refine this procedure by measuring the phase lag for each data set and aligning that lag precisely with the Q-axis.

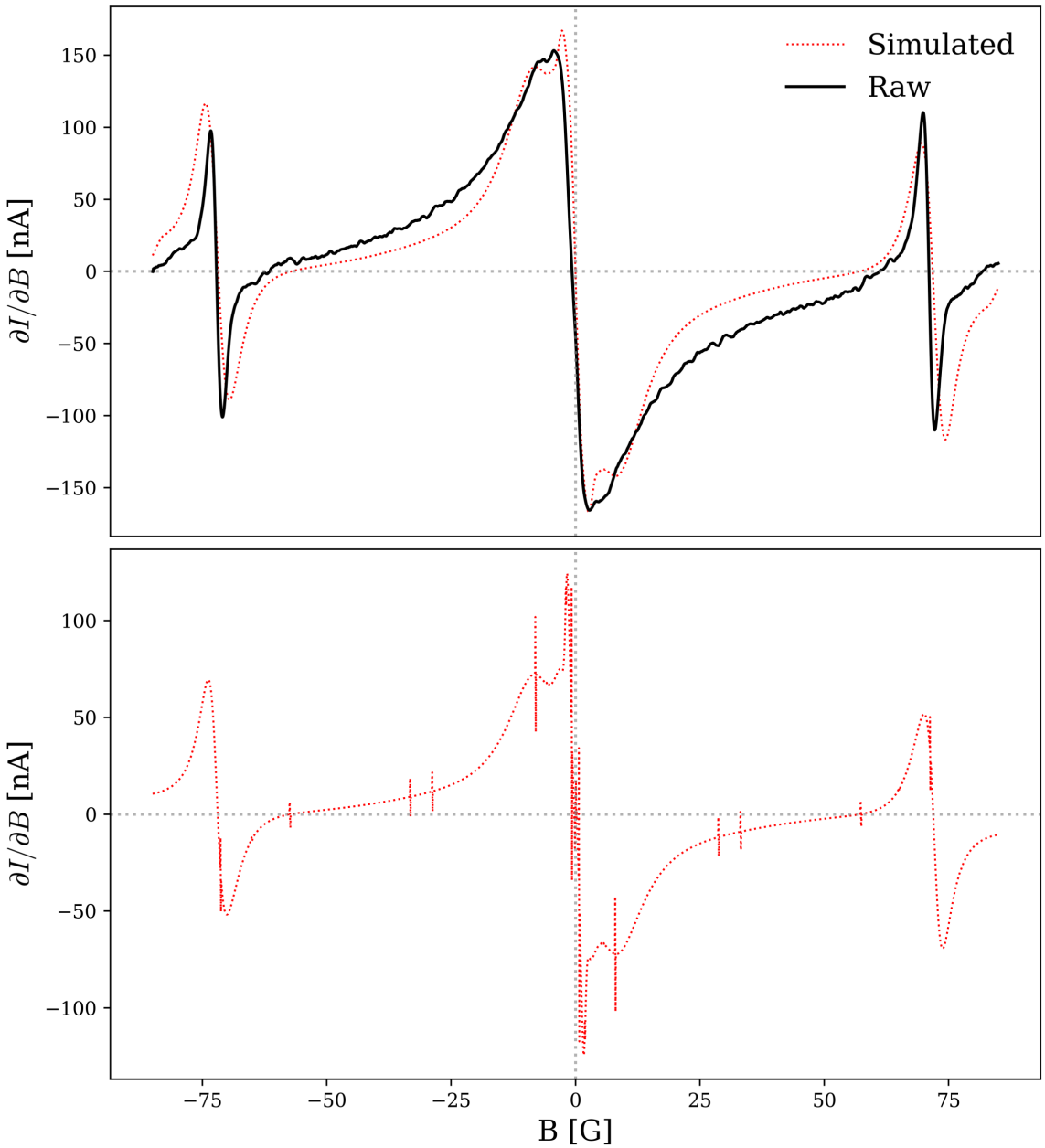

Figure 1. **Top:** Simulated EDMR first-harmonic derivative (red dotted) overlaid with the measured spectrum (black) from a 4H-SiC V_{Si}^{-} diode at 3 V bias, 200 MHz excitation, and 2 G peak-to-peak field modulation. **Bottom:** Unmodulated simulated EDMR derivative revealing primary features of the V_{Si}^{-} spectrum before lock-in convolution. The zero-field singlet–triplet crossing dominates at $B = 0$, followed by sharp exchange-mixed spikes near ± 15 G, the forbidden half-field transition at ~ 35 G, and the resonances at ~ 71.4 G.

3.2 Line-shape fitting and signal parameters

To extract the amplitude, linewidth, and center field of the main resonance signal and two weak hyperfine satellites, we fit each spectrum to

$$\frac{\partial I}{\partial B} = \sum_{k=0}^{2} A_k \frac{d}{dB}\mathcal{L}\big(B - B_k, \Gamma_k\big) + mB + c,$$

where the first term is a sum of three Lorentzian derivatives (main transition feature + two hyperfine satellites) and $mB + c$ is a linear baseline.

3.3 RF-power series

We collected spectra at $\nu = 200.42\,\mathrm{MHz}$ and 11 dBm to 23 dBm (12.59 mW to 199.53 mW) RF power using a DOTY Scientific loop coil (8 mm diameter, $\pi/2$ pulse 7.6μs for ^{1}H at full power). We fitted the curve composed of three Lorentzian derivatives and a linear baseline using an analysis of peaks in the third derivative of the lineshape to select initial guesses for the signal fitting. Across the 13 RF power settings we examined, the coefficient of determination stays tightly clustered in the range $R^2 = 0.998$–0.999. The consistently high R^2 values confirm that our fitted model accurately reproduces the observed line shapes (see Figure 2 for an example fit).

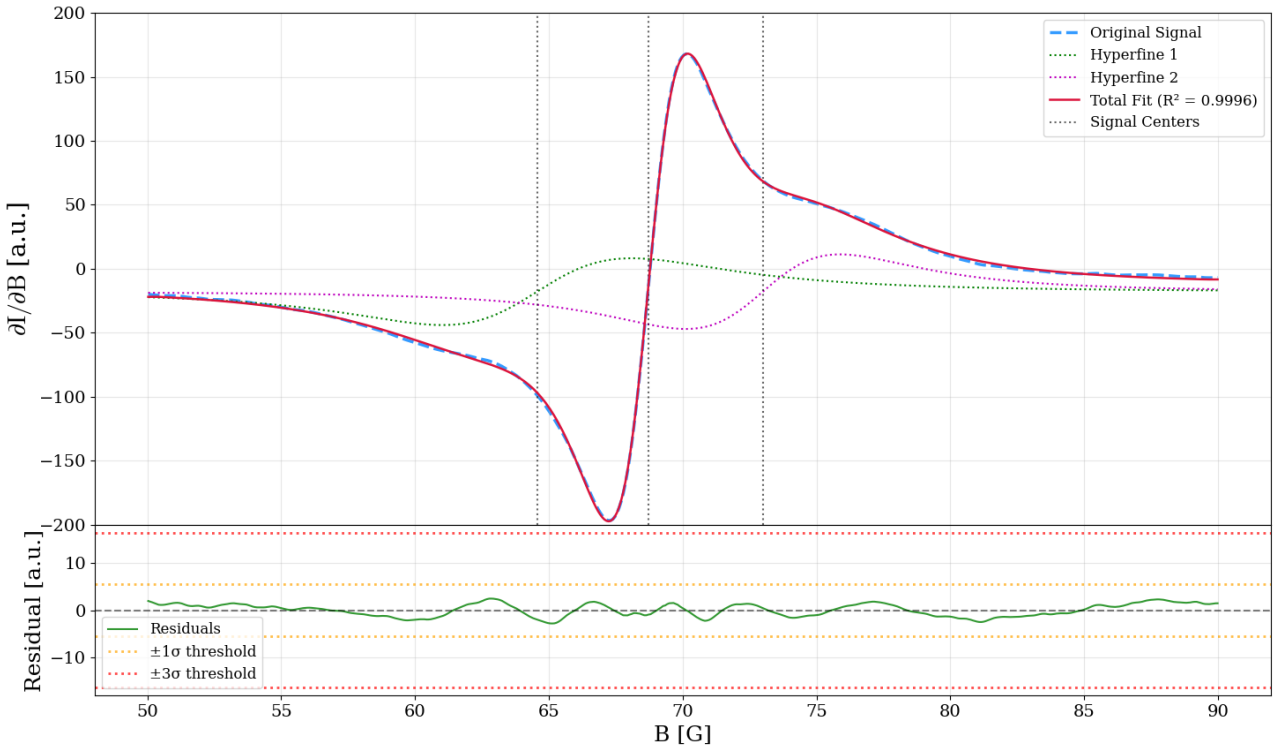

Figure 2. A plot of the total fit produced by our method is overlaid on top of the original signal, both of which include the effects of the main resonance transition and the hyperfine signals, which are also displayed separately. The hyperfine signal centers are approximately symmetric around the main signal's center. We used a 2 G modulation amplitude, a 1.25 kHz modulation frequency, and in the case of this particular fit, an RF power of 23 dBm.

The fitted parameters demonstrate an expected power saturation curve where the amplitude of the main resonance signal stops increasing at higher RF powers (see Figure 3). The linewidth parameters also demonstrate the effect of power broadening.

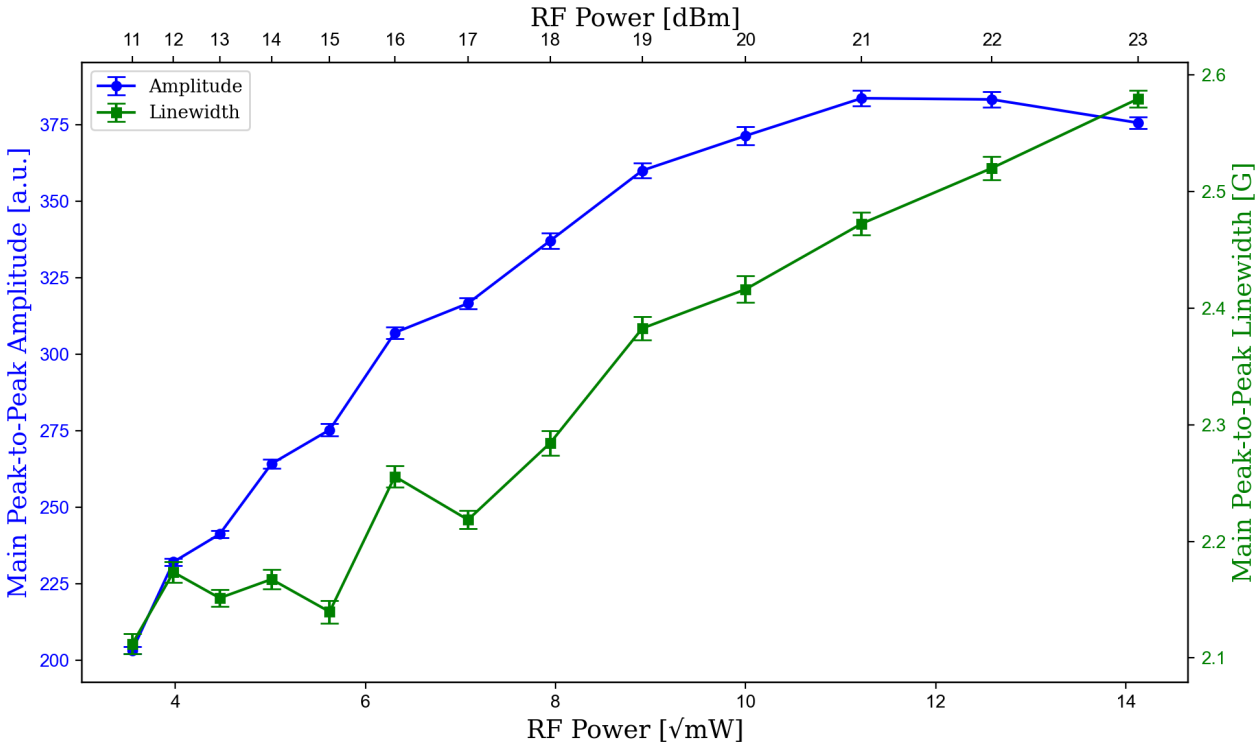

Figure 3. The peak-to-peak amplitude of the main resonance signal is plotted with respect to RF power. The amplitude increase steadily then plateaus and begins to decrease slightly with power broadening, which itself is illustrated by a plot of peak-to-peak linewidth of the same signal. We see that the ideal operating condition to maximize signal while minimizing this power broadening for our device is an RF power of approximately 21 dBm.

4. MAGNETIC FIELD SENSITIVITY

4.1 Magnetic-field sensitivity at the NZFMR zero crossing

NZFMR lends itself naturally to quantum-magnetometry because the measurement is reduced to tracking the slope of a current–field dispersion at a single zero crossing (Figure 4a). For a spin-pair ensemble with a Gaussian current profile [3,31]

$$I(B) = \frac{\Delta I}{\sigma\sqrt{2\pi}} \exp\!\left(-\tfrac{B^2}{2\sigma^2}\right), \tag{7}$$

the key figures of merit are σ, the r.m.s. linewidth (in T), ΔI, the line amplitude (in A), and B, the external field referenced to the center at $B = 0$.

Lock-in detection. The sinusoidal field modulation is proportional to the derivative $\partial I/\partial B$ provided $B_{\mathrm{mod}} \ll \sigma$ (Equation (6)). Demodulating that component therefore yields a voltage whose envelope tracks the local slope at the zero crossing (Figure 4a, inset). The useful bandwidth Δf is set by the low-pass time constant τ that follows the mixer in the lock-in chain (Figure 4b).

Shot-noise–limited sensitivity. Because the field modulation moves the signal away from low-frequency flicker noise, the ultimate noise floor is set by shot noise in the DC transport current I_0. Propagating that noise through the demodulation chain gives the field-equivalent noise density [3]

$$\frac{\delta B}{\sqrt{\Delta f}} = 2\sqrt{\pi q}\,\frac{\sigma^3}{B_{\mathrm{mod}}^2}\,\frac{\sqrt{I_0}}{\Delta I} \tag{8}$$

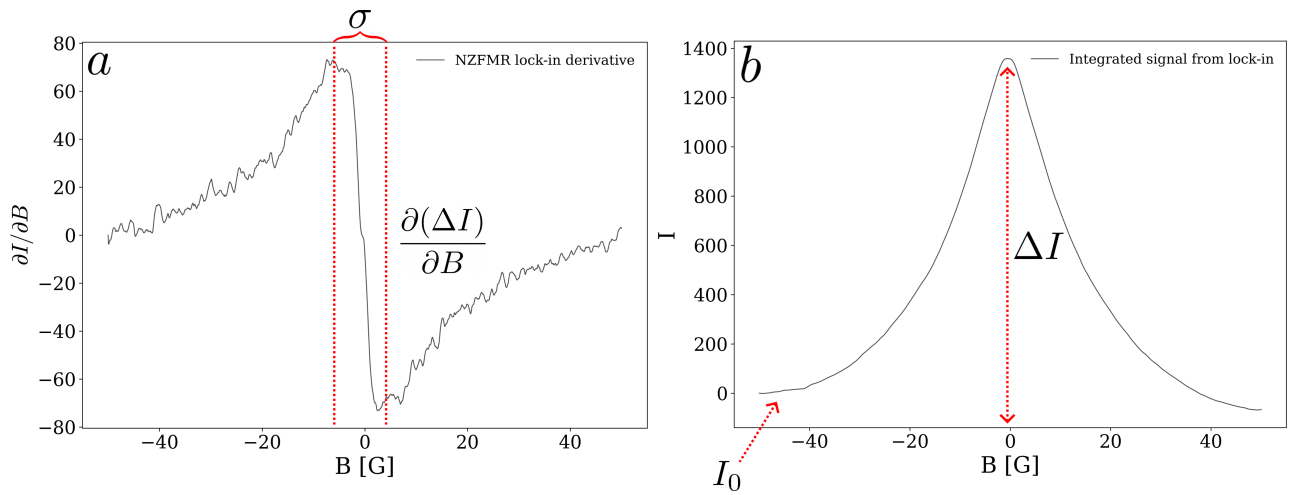

Figure 4. **(a)** First-harmonic NZFMR derivative recorded with a lock-in amplifier. The Gaussian linewidth σ that enters Equation (8) is extracted from this trace. **(b)** Spectrum obtained by numerically integrating the derivative, revealing the signal amplitude ΔI and the DC baseline I_0. Together with the modulation amplitude B_{mod}, these values set the shot-noise-limited sensitivity in Equation (8).

where q is the elementary charge. Using parameters extracted from Figure 4 (σ, ΔI, I_0) and $B_{\mathrm{mod}} = 2\,\mathrm{G}$, we obtain a shot-noise-limited sensitivity of $\delta B = 13.2\,\mathrm{nT}/\sqrt{\mathrm{Hz}}$.

Generality and external factors. Zero-field spin mixing is a generic result of spin-dependent transport involving an electron–hole (or defect–electron) pair coupled to nearby nuclear spins and has been observed in a variety of mechanisms [33-36]. Specific details of the transport channel alter the NZFMR response and therefore modify σ and ΔI, directly affecting sensitivity [37]. External parameters such as temperature and electric field can also perturb the spin-pair Hamiltonian, leading to measurable shifts in both the linewidth and the amplitude; these dependencies provide additional knobs for optimizing quantum-magnetometer performance.

5. SUMMARY AND OUTLOOK

Near–zero-field magnetoresistance (NZFMR) in the silicon vacancy of 4H-SiC provides a natural zero crossing from which to read out magnetic fields with high precision. In this work we showed that a *resonance-to-resonance* simulation, built from a sixteen-dimensional spin Hamiltonian and solved with an accelerated Lyapunov approach, reproduces primary features of observed electrically-detected EDMR spectra, including the NZFMR zero-field peak, theoretical exchange-mixed spikes at ±15 G, the half-field, and the Zeeman resonances at ±71.4 G. By matching experiment and theory in both amplitude and rough line shape, the model yields physically grounded description of *spin-dependent recombination* (SDR) across the entire spectrum. We attribute the residual mismatch between our simulated and experimental spectra to additional spin-dependent processes, most likely *spin-dependent trap-assisted tunneling* (SDTAT) [38], that are not yet included in the SDR model. Developing a dedicated SDTAT simulation alongside our SDR framework will not only quantify the individual contributions of each mechanism, but will also lay the foundation for a unified and comprehensive model. Such a model is essential for disentangling the intrinsic spin-physics parameters (e.g. hyperfine, splitting, exchange coupling) from extrinsic influences on the zero-field response, notably temperature and applied electric field. A clear separation of these factors is the key to engineering SiC magnetometers whose performance is limited only by shot noise.

To isolate weak hyperfine signals and the main transition signal, we introduced a phase-optimized lock-in workflow that rotates the raw I–Q data onto the true signal axis with principal component analysis, relegating RF-heating artifacts to the quadrature channel. A three-component Lorentzian derivative model with a linear baseline fits the data with coefficients of determination clustered within the range 0.98 to 0.99 over the 11 dBm to 23 dBm power range, confirming that the essential spin physics is captured. Power-dependent measurements

revealed a significant broadening of the central linewidth, identifying an operating window near 21 dBm that maximizes contrast without excessive distortion. Using the measured linewidth σ, amplitude ΔI, dc current I_0, and a 2 G modulation field, Equation 8 predicts a shot-noise-limited magnetic-field sensitivity of $\delta B = 13.2\,\mathrm{nT\,Hz^{-1/2}}$, an order-of-magnitude improvement over previous room-temperature, all-electrical SiC sensors.

Looking ahead, a comprehensive map of the zero-field line shape versus temperature, bias electric field, and defect concentration will allow intrinsic and extrinsic contributions to be disentangled with even higher accuracy. Coupling those measurements with the simulation framework presented here will clarify the full role of spin-dependent recombination in SiC and guide the design of next-generation, fully integrated, radiation-hard quantum magnetometers for heliophysics, planetary exploration, and biomedical diagnostics.

Data Availability

The data for plots and code for simulating EDMR is available upon reasonable requests.

ACKNOWLEDGMENTS

We would like to thank Drs. Jesse Berevosky and Gary Hunter for their content discussions and suggestions. This material is primarily supported by NASA Glenn Research Center's Science Mission Directorate (SMD) and partially based on work supported by the U.S. Department of Energy, Office of Science, Office of Advanced Scientific Computing Research (ASCR), Reaching a New Energy Sciences Workforce (RENEW) under award number [DE-SC0024219].

6. REFERENCES

[1] D. R. Hart, D. J. Spry, A. A. Sissay, K. N. Burgess, and K. Maeda, "Icing mitigation through quantum sensing," Proc. SPIE 12656, Spintronics XVI, 126560P (2023).

[2] J. M. McCoey, M. Matsuoka, R. W. de Gille, *et al.*, "Quantum magnetic imaging of iron biomineralization in teeth of the chiton *Acanthopleura hirtosa*," Small Methods 4(3), 1900754 (2020).

[3] C. J. Cochrane, J. Blacksberg, M. A. Anders, and P. M. Lenahan, "Vectorized magnetometer for space applications using electrical readout of atomic-scale defects in silicon carbide," Sci. Rep. 6, 37077 (2016).

[4] C. J. Cochrane, H. Kraus, P. G. Neudeck, *et al.*, "Magnetic field sensing with 4H-SiC diodes: N vs. P implantation," Mater. Sci. Forum 924, 988–992 (2018).

[5] S. Castelletto and A. Boretti, "Silicon carbide color centers for quantum applications," J. Phys. Photonics 2(2), 022001 (2020).

[6] A. Bourassa, C. P. Anderson, K. C. Miao, *et al.*, "Entanglement and control of single nuclear spins in isotopically engineered silicon carbide," Nat. Mater. 19(12), 1319–1325 (2020).

[7] D. J. Christle, A. L. Falk, P. Andrich, *et al.*, "Isolated electron spins in silicon carbide with millisecond coherence times," Nat. Mater. 14(2), 160–163 (2015).

[8] D. Riedel, F. Fuchs, H. Kraus, *et al.*, "Resonant addressing and manipulation of silicon vacancy qubits in silicon carbide," Phys. Rev. Lett. 109(22), 226402 (2012).

[9] S. G. Carter, Ö. O. Soykal, P. Dev, S. E. Economou, and E. R. Glaser, "Spin coherence and echo modulation of the silicon vacancy in 4H-SiC at room temperature," Phys. Rev. B 92(16), 161202 (2015).

[10] N. Mizuochi, S. Yamasaki, H. Takizawa, *et al.*, "Continuous-wave and pulsed EPR study of the negatively charged silicon vacancy with $S = 3/2$ and C_{3v} symmetry in n-type 4H-SiC," Phys. Rev. B 66(23), 235202 (2002).

[11] A. Chatterjee, P. Stevenson, S. De Franceschi, *et al.*, "Semiconductor qubits in practice," Nat. Rev. Phys. 3(3), 157–177 (2021).

[12] A. J. Fallon, D. R. Hart, E. J. Katz, B. E. Vyhnalek, I. A. Chin, and J. D. Lekki, "Dual-fiber spectrometer for a highly non-degenerate entanglement source," Proc. SPIE 12446, Quantum Computing, Communication, and Simulation III, 124460X (2023).

[13] A. Lohrmann, T. J. Karle, V. K. Sewani, *et al.*, "Integration of single-photon emitters into 3C-SiC microdisk resonators," ACS Photonics 4(3), 462–468 (2017).

[14] B. B. Goldberg, S. B. Ippolito, L. Novotny, Z. Liu, and M. S. Unlu, "Immersion-lens microscopy of photonic nanostructures and quantum dots," IEEE J. Sel. Top. Quantum Electron. 8(5), 1051–1059 (2002).

[15] A. Lohrmann, N. Iwamoto, Z. Bodrog, *et al.*, "Single-photon emitting diode in silicon carbide," Nat. Commun. 6, 7783 (2015).

[16] A. Lohrmann, B. C. Johnson, J. C. McCallum, and S. Castelletto, "A review on single-photon sources in silicon carbide," Rep. Prog. Phys. 80(3), 034502 (2017).

[17] B. C. Johnson, J. Wörle, D. Haasmann, *et al.*, "Optically active defects at the SiC/SiO_2 interface," Phys. Rev. Appl. 12(4), 044024 (2019).

[18] M. A. Anders, P. M. Lenahan, and A. J. Lelis, "Multi-resonance frequency spin-dependent charge pumping and spin-dependent recombination applied to the 4H-SiC/SiO_2 interface," J. Appl. Phys. 122(23), 234503 (2017).

[19] M. A. Anders, P. M. Lenahan, N. J. Harmon, and M. E. Flatté, "Near-zero-field spin-dependent charge pumping at the MOSFET interface," J. Appl. Phys. 128(24), 244501 (2020).

[20] A. Schweiger and G. Jeschke, *Principles of Pulse Electron Paramagnetic Resonance*, Oxford University Press, Oxford (2001).

[21] D. J. Lépine, "Spin-dependent recombination on silicon surfaces," Phys. Rev. B 6, 436–441 (1972).

[22] D. Kaplan, I. Solomon, and N. F. Mott, "Explanation of the large spin-dependent recombination effect in semiconductors," J. Phys. Lett. 39, L51–L54 (1978).

[23] D. R. McCamey, H. Huebl, M. S. Brandt, *et al.*, "Electrically detected magnetic resonance in ion-implanted Si:P nanostructures," Appl. Phys. Lett. 89, 182115 (2006).

[24] F. Sgrignuoli, I. Viti, Z. G. Yu, *et al.*, "All-electrical near-zero-field magnetoresistance magnetometry up to 500 °C using SiC devices," arXiv:2411.15196 (2025).

[25] Ö. O. Soykal, P. Dev, and S. E. Economou, "Silicon vacancy center in 4H-SiC: Electronic structure and spin–photon interfaces," Phys. Rev. B 93, 081207 (2016).

[26] A. L. Falk, B. B. Buckley, G. Calusine, *et al.*, "Polytype control of spin qubits in silicon carbide," Nat. Commun. 4, 1819 (2013).

[27] M. Niethammer, M. Widmann, S.-Y. Lee, *et al.*, "Vector magnetometry using silicon vacancies in 4H-SiC under ambient conditions," Phys. Rev. Appl. 6, 034001 (2016).

[28] T. Hansen and N. L. Pedersen, "Spin-dependent recombination studied by steady-state stochastic Liouville theory," Chem. Phys. Lett. 363, 636–642 (2002).

[29] H. W. Kuhn, "The Hungarian method for the assignment problem," Nav. Res. Logist. Q. 2(1–2), 83–97 (1955).

[30] C. J. Cochrane, P. M. Lenahan, and A. J. Lelis, "Identification of a silicon vacancy as an important defect in 4H-SiC MOSFETs using spin-dependent recombination," Appl. Phys. Lett. 100(2), 023509 (2012).

[31] J. Yoneda, T. Otsuka, T. Nakajima, T. Takakura, T. Obata, M. Pioro-Ladrière, H. Lu, C. J. Palmstrøm, A. C. Gossard, *et al.*, "Fast Electrical Control of Single Electron Spins in Quantum Dots with Vanishing Influence from Nuclear Spins," Phys. Rev. Lett. 113, 267601 (2014).

[32] W. J. Baker, K. Ambal, D. P. Waters, *et al.*, "Robust absolute magnetometry with organic thin-film devices," Nat. Commun. 3, 898 (2012).

[33] P. Klemm, S. Bange, A. Pöllmann, C. Boehme, and J. M. Lupton, "Nanotesla magnetoresistance in π-conjugated polymer devices," Phys. Rev. B 95(24), 241407 (2017).

[34] F. L. Bloom, W. Wagemans, M. Kemerink, and B. Koopmans, "Correspondence of the sign change in organic magnetoresistance with the onset of bipolar charge transport," Appl. Phys. Lett. 93(26), 04449 (2008).

[35] A. J. Schellekens, W. Wagemans, S. P. Kersten, P. A. Bobbert, and B. Koopmans, "Microscopic modeling of magnetic-field effects on charge transport in organic semiconductors," Phys. Rev. B 84(7), 075204 (2011).

[36] T. D. Nguyen, G. Hukic-Markosian, F. Wang, *et al.*, "Isotope effect in spin response of π-conjugated polymer films and devices," Nat. Mater. 9(4), 345–352 (2010).

[37] C. J. Cochrane and P. M. Lenahan, "Zero-field detection of spin-dependent recombination with direct observation of electron–nuclear hyperfine interactions in the absence of an oscillating electromagnetic field," J. Appl. Phys. 112(12), 123714 (2012).

[38] J. T. Ryan, P. M. Lenahan, A. T. Krishnan, S. Krishnan, *et al.*, "Energy resolved spin dependent trap-assisted tunneling investigation of SILC related defects," in 2010 IEEE International Reliability Physics Symposium, IRPS 2010, pp. 1122–1125 (2010).